Published on 27 January 2020. Downloaded by Changchun Institute of Optics, Fine Mechanics and Physics, CAS on 4/7/2021 8:22:32 AM.

Journal of Materials Chemistry A

ROYAL SOCIETY OF CHEMISTRY

PAPER

View Article Online
View Journal | View Issue

Check for updates

Cite this: J. Mater. Chem. A, 2020, 8, 4040

Dual LSPR of Au/$W_{18}O_{49}$ heterostructures for upconversion enhancement and application of molecular detection†

Yang Yang, [ab] Yan Cong,*[a] Xiang Lin,[a] Baosheng Cao, [a] Dapeng Dong,[a] Kuichao Liu,[a] Yu Xiao, [c] Jingyu Shang,[a] Yanan Bao,[a] Yang Liu,[a] Guoqiang Fang,[a] Yue Wang,[a] Yongqi Chen,[a] Jiahua Zhang *[b] and Bin Dong *[a]

Received 9th December 2019
Accepted 27th January 2020

DOI: 10.1039/c9ta13466b

rsc.li/materials-a

A nano-heterostructure composed of the noble metal Au and the semiconductor $W_{18}O_{49}$ enhances the localized electric field due to the strong coupling of localized surface plasmon resonance (LSPR). The Au/$W_{18}O_{49}$ nano-heterostructures have been further explored to enhance the upconversion luminescence (UCL) of $NaYF_4$:Yb,Er nanoparticles. An enhancement up to 1108-fold is achieved for the overall UCL intensity of Er^{3+}, which is primarily due to the improvement of the excitation field and partly due to the coupling of LSPR with emission light. Finally, based on the intense UCL caused by the excellent synergetic LSPR, a dual detection method of qualitative before quantitative detection of rhodamine 6G (R6G) using SERS signal monitoring and fluorescence sensing is established. This novel detection method with a high sensitivity of 10^{-11} M (100 aM), a good linear relationship and a wide concentration range of 10^{-11} M to 10^{-3} M can potentially be applied in accurate molecular detection.

Introduction

Localized surface plasmon resonance (LSPR) of noble metals and some heavily doped semiconductor nanostructures with fascinating photophysical phenomena has attracted significant interest in research areas such as electronics, photonics, catalysis, biology and sensing.[1–6] Upon resonance, the electric field at the surface of the nanoparticle is strongly enhanced, resulting in molecules in the vicinity exhibiting enhanced absorption and emission, Raman scattering, and nonlinear optical properties. Surface-enhanced Raman scattering (SERS) which can provide fingerprint information with high sensitivity has been widely studied for application as an ultrasensitive spectroscopic tool for the detection of low-abundance analytes.[7,8] More recent studies have focused on intense localized electric field enhancement exploitable for SERS-based molecular characterization and sensing applications. Surprising research results such as a low detection limit of 10^{-16} M for rhodamine 6G (R6G) are obtained by SERS analysis.[9–11] Despite a low detection limit being consistently achieved, the quantitative comparison of the SERS intensities as a function of analyte concentration demonstrates a linear concentration range from about 10^{-10} to 10^{-7} M as a general result in the literature.[9,12] This makes the SERS-based detection applicable for quantitative detection of analyte molecules in a narrow concentration window.

Rare-earth doped upconversion nanoparticles (UCNPs) have attracted much attention because of the unique optical properties and great application in biological imaging, solar cells, fluorescent probes and other fields.[13–18] During the development of its application, the detection of UC fluorescent probes based on fluorescence resonance energy transfer and specific interaction was conducted.[16–20] UC fluorescent sensors have advantages such as small molecular volume, good biocompatibility, high sensitivity and good linear relationship, and thus may be used in quantitative biodetection. The sweeping applications of UCNPs in fluorescent probes have made researchers realize the importance of improving UCL efficiency.[21–24] LSPR has been employed to improve the UC efficiency and further increase the detection sensitivity of fluorescent molecular probes.[25,26] Classic noble metals have light trapping ability only in the visible region and within a narrow range, which cannot simultaneously match the excitation and emission bands of UCNPs.[27–29] In recent years, LSPR has been observed in some heavily doped semiconductor nanostructures, such as $Cu_{2-x}S$, Sn-doped In_2O_3, WO_{3-x}, and MoO_{3-x}. Heavily doped semiconductors generally have a lower density of free charge carriers than noble metals

[a]Key Laboratory of New Energy and Rare Earth Resource Utilization of State Ethnic Affairs Commission, Dalian Minzu University, Dalian 11660, China. E-mail: congyan@dlnu.edu.cn; dong@dlnu.edu.cn

[b]State Key Laboratory of Luminescence and Applications, Changchun Institute of Optics, Fine Mechanics and Physics, Chinese Academy of Sciences, 3888, Eastern South Lake Road, Changchun 130033, China. E-mail: zhangjh@ciomp.ac.cn

[c]Department of Applied Physics, College of Science, Nanjing Forestry University, Nanjing 210037, China

† Electronic supplementary information (ESI) available. See DOI: 10.1039/c9ta13466b

This journal is © The Royal Society of Chemistry 2020

Published on 27 January 2020. Downloaded by Changchun Institute of Optics, Fine Mechanics and Physics, CAS on 4/7/2021 8:22:32 AM.

and as a result exhibit longer-wavelength (lower energy) LSPR.[30–32] Such optical features make plasmonic semiconductors a potential choice for coupling with noble metal nanostructures, and the optical properties of these metal–semiconductor heterostructures will differ substantially from the sum of those of their components. Here, we utilize the dual plasmonic mode generated by Au/$W_{18}O_{49}$ heterostructures as optical antennae to enhance the UCL in a multilayer-structured film consisting of $NaYF_4$ nanoparticles (NPs) as the luminescent layer. The hybridization of Au nanorods (NRs) and $W_{18}O_{49}$ nanowires (NWs) synergistically improves the electric field environment around UCNPs to overcome the limitations of a single LSPR mode, raising the UCL enormously. Another key design characteristic of the $NaYF_4$/Au/$W_{18}O_{49}$ multilayer-structured composite film is its ability to achieve SERS enhancement simultaneously. Using this unique feature, we develop a novel R6G molecule detection process, which achieves qualitative to quantitative detection with high sensitivity by using SERS signal monitoring and UC fluorescence sensing.

Results and discussion

As schematically shown in Fig. 1A, the plasmonic composite film of $NaYF_4$ NPs/Au NRs/$W_{18}O_{49}$ NWs is prepared by simple self-assembly. First, $W_{18}O_{49}$ NWs are grown on FTO glass to achieve a single plasmonic layer *via* the solvothermal process. Next, random assembly of Au NRs onto the $W_{18}O_{49}$ NW layer surface forms the Au NRs/$W_{18}O_{49}$ NW heterostructure film through a solvent evaporation process. Based on a similar fabrication method, $NaYF_4$ NPs are self-assembled on the top surface of the Au/$W_{18}O_{49}$ plasmonic composite film, forming the UCL layer. Scanning electron microscopy (SEM) images show the side views of the above films (Fig. 1B). It can be seen that the $W_{18}O_{49}$ NWs align in random orientations on the FTO glass like a patch of greensward. The Au NRs and the $NaYF_4$ NPs are densely distributed and intercalated into the $W_{18}O_{49}$ NWs hierarchically forming the $NaYF_4$/Au/$W_{18}O_{49}$ multilayer structure (see the locally magnified views). The randomly tilted growth of $W_{18}O_{49}$ NWs on the film enabled the majority of self-assembled Au NRs to directly come into contact with the side

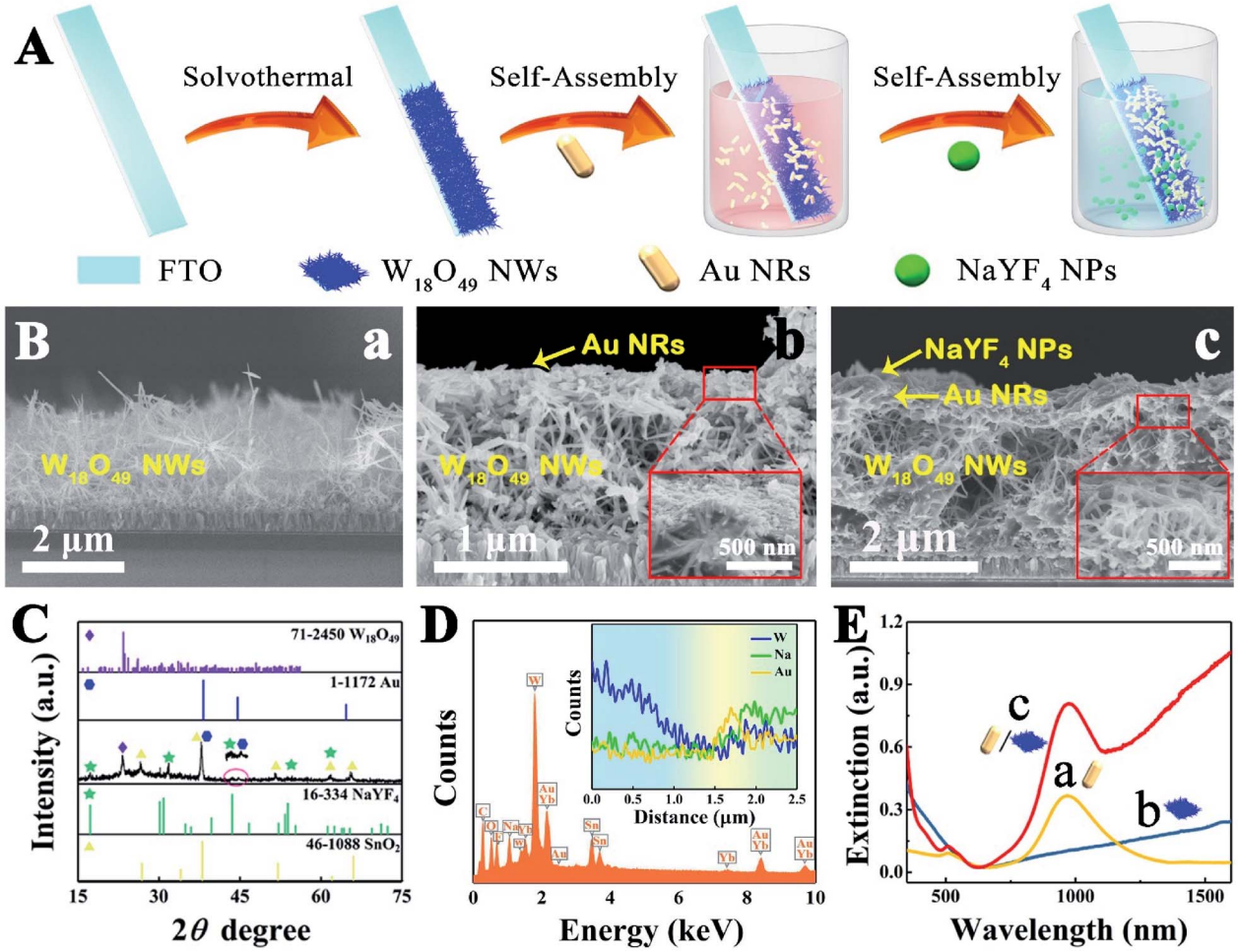

Fig. 1 (A) Schematic of the formation process of the $NaYF_4$ NPs/Au NRs/$W_{18}O_{49}$ NW hybrid film. (B) SEM images of the side view of the $W_{18}O_{49}$ NW film (a), side view and locally magnified view of Au NRs deposited on the $W_{18}O_{49}$ NW film (b), and side view and locally magnified view of $NaYF_4$ NPs deposited on the Au NRs/$W_{18}O_{49}$ NW film (c). (C) XRD patterns and (D) EDS pattern of the $NaYF_4$ NPs/Au NRs/$W_{18}O_{49}$ NW composite film; the inset shows the elemental distributions of the $NaYF_4$/Au/$W_{18}O_{49}$ composite film depending on the depth along the vertical direction of the film. (E) Extinction spectra of the Au NRs (a), $W_{18}O_{49}$ NWs (b), and Au NRs/$W_{18}O_{49}$ NWs (c).

Published on 27 January 2020. Downloaded by Changchun Institute of Optics, Fine Mechanics and Physics, CAS on 4/7/2021 8:22:32 AM.

surface of the $W_{18}O_{49}$ NWs, which is helpful for the formation of interactions between the two domains in the Au/$W_{18}O_{49}$ heterostructures. To show more accurate distributions between the $W_{18}O_{49}$, Au and $NaYF_4$ within the synthesized composite film, the elemental mapping images of a cross-section of $NaYF_4$/Au/$W_{18}O_{49}$ are also given in Fig. S1, ESI.† The X-ray diffraction (XRD) patterns (Fig. 1C) confirm that the composite luminescent film consists of $W_{18}O_{49}$, Au and β-$NaYF_4$ phases, and the diffraction peaks of SnO_2 are ascribed to the FTO glass substrate. No secondary phase is observed in this film, demonstrating that there is no interaction among the respective three layers. The above results can also be confirmed through the elemental composition obtained by performing energy dispersive spectrometry (EDS) for the hybrid film, where $NaYF_4$ NPs/Au NRs/$W_{18}O_{49}$ NWs are assuredly extant, and Er^{3+} cannot be distinguished using this system because of its low doping content (Fig. 1D). The elemental distributions in the corresponding cross sectional SEM image of the $NaYF_4$/Au/$W_{18}O_{49}$ composite film are obtained through EDS and indicate that the $NaYF_4$ and Au are in direct contact with the $W_{18}O_{49}$ NWs to form a heterostructure layer with a depth of about 1 μm on the top surface of the film. Fig. 1E shows the comparison of extinction spectra of the Au NRs/$W_{18}O_{49}$ NW composite film and individual Au NRs and $W_{18}O_{49}$ NWs films. The extinction spectrum of the Au NR film exhibits a longitudinal (L-) LSPR peak at 980 nm, while the $W_{18}O_{49}$ NW film shows an intense LSPR band across the visible and NIR region. Interestingly, the curve profile of the Au/$W_{18}O_{49}$ composite film is not the summation curves of the LSPR bands between the Au NR and $W_{18}O_{49}$ NW films, and the composite dual LSPR band not only further elevates the extinction intensity of noble metal nanoparticles, but also exhibits an extensive extinction range for the plasmonic semiconductor. These results suggest that double plasmonic-coupling occurs in the Au NRs/$W_{18}O_{49}$ NW composite film, and it simultaneously shows two types of LSPR in a single system.

Under the irradiation of incident light, a strong excitation field is generated around the Au NRs/$W_{18}O_{49}$ NW coupled system, which interacts with the adjacent UC light field, thereby increasing the luminescence intensity (Fig. 2A). Tuning the LSPR peak to match the excitation field tends to better enhance the UCL,[33,34] and thus the desired enhancement effect for UCL is

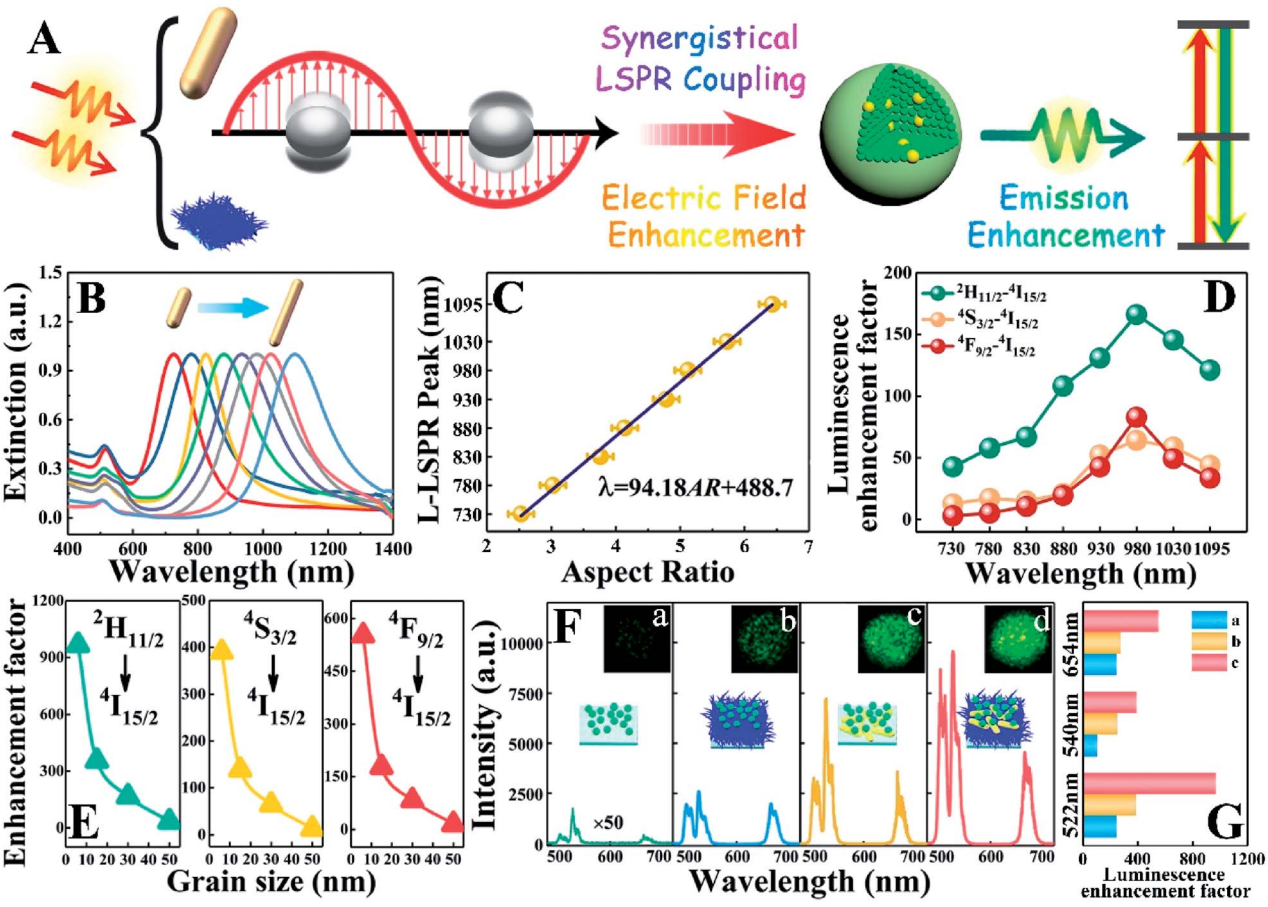

Fig. 2 (A) The schematic diagram of plasmonic enhancement of UCL. (B) Extinction spectra depending on the aspect ratio of Au NRs. (C) Calibration curve between the experimental L-LSPR peak position and the aspect ratio of Au NRs. (D) Dotted line diagram of enhancement factors of different transitions as a function of the L-LSPR peak of Au NRs in the $NaYF_4$/Au/$W_{18}O_{49}$ film. (E) Luminescence enhancement factors of different transitions as a function of the grain sizes of $NaYF_4$ NPs. (F) UC emission spectra of the (a) $NaYF_4$, (b) $NaYF_4$/$W_{18}O_{49}$, (c) $NaYF_4$/Au, and (d) $NaYF_4$/Au/$W_{18}O_{49}$ films. (G) UCL enhancement factors of the (a) $NaYF_4$/$W_{18}O_{49}$, (b) $NaYF_4$/Au, and (c) $NaYF_4$/Au/$W_{18}O_{49}$ films.

 This journal is © The Royal Society of Chemistry 2020

Published on 27 January 2020. Downloaded by Changchun Institute of Optics, Fine Mechanics and Physics, CAS on 4/7/2021 8:22:32 AM.

achieved through making targeted specific adjustments depending on the peak position of the excitation light. The L-LSPR of Au NRs is precisely adjusted from 780 to 1095 nm by controlling the aspect ratio of Au NRs during the experiment (Fig. S2, ESI†). As the aspect ratio increases, the L-LSPR wavelength of Au NRs undergoes a red shift phenomenon (from 730 nm to 780 nm, 830 nm, 880 nm, 930 nm, 980 nm, 1030 nm, and 1095 nm), while the transverse wavelength shows little dependence on the aspect ratio (Fig. 2B). We find that the L-LSPR peak exhibits a normalized linear relationship with the aspect ratio of Au NRs as shown in Fig. 2C, which could be regressed as $\lambda = 98.14AR + 488.7$, where λ is the L-LSPR peak position and *AR* is the aspect ratio value. Subsequently, Au NRs with different L-LSPR peaks are assembled on the surface of the semiconductor $W_{18}O_{49}$ NW films to form Au/$W_{18}O_{49}$ heterostructure films. $NaYF_4$:Er^{3+},Yb^{3+} NPs are selected as a model emitter to approach the plasmonic nanostructure in the UCL experiments. Typical green emission ($^2H_{11/2}$,$^4S_{3/2}$-$^4I_{15/2}$ transitions) and red emission ($^4F_{9/2}$-$^4I_{15/2}$ transition) from Er^{3+}-Yb^{3+} are shown in the UC emission spectra (see Fig. 2F(a)). Just as expected, the UCL intensity exhibits a dramatic improvement when the emitters approach the Au/$W_{18}O_{49}$ nanoheterostructures *via* plasmonic energy transfer. The enhancement factors as a function of L-LSPR peak position of Au NRs in the $NaYF_4$/Au/$W_{18}O_{49}$ hybrid film at different emission wavelengths are shown in Fig. 2D. As is evident from Fig. 2D, the enhancement factors of UCL for different aspect ratios of Au NRs show large variation. When precisely tuning the L-LSPR position to the same wavelength as the incident light (980 nm), the UCL enhancement factors reach their maximum at all the three emission wavelengths.

The strong double effect occurs when the noble metal Au NRs are assembled on the surface of the semiconductor $W_{18}O_{49}$ NW layer, representing an enhanced and widened LSPR band. In the case of the extinction spectrum of the Au NRs/$W_{18}O_{49}$ NW composite film (Fig. 1E), the LSPR peak of Au NRs is located at approximately 980 nm, matching the wavelength of the pumping light of UC well. After the formation of the Au/$W_{18}O_{49}$ heterostructure film, we optimize the UC luminescent layer based on the luminescence enhancement principle. The area of the LSPR-induced near-field effect is quite limited, so emitters of different sizes are prepared, and UC emission dependence on the emitter size is explored. The $NaYF_4$ NPs with a singly-dispersed and homogeneous nanostructure (6 nm, 15 nm, 30 nm, and 50 nm) are used to demonstrate the coupling effect of dual LSPR through fluorescence measurement under the same excitation power and test parameters (Fig. S3, ESI†). The UCL intensity of the 6 nm $NaYF_4$ NPs is the weakest among those of all the $NaYF_4$ NP samples (Fig. S4, ESI†), which is mainly due to the effect of surface defects in nanocrystals, to our knowledge. On the other hand, the effective interaction distance for the LSPR-enhanced near-field effect is limited. The decrease in particle size ensures that most of the luminescent centers are positioned within the effective interaction distance, inducing a more effective enhancement of UCL. So the optimal UCL enhancement factor is achieved in the case of 6 nm $NaYF_4$ NPs after plasmonic sensitization *via* the Au/$W_{18}O_{49}$ plasmonic composite film, and then the enhancement factor decreases sharply with the increasing size as shown in Fig. 2E. Although 6 nm $NaYF_4$ NPs exhibited an optimal enhancement factor, 15 nm $NaYF_4$ NPs show the largest UCL intensity after coupling with Au/$W_{18}O_{49}$ in our work (Fig. S4, ESI†).

To investigate the synergistic LSPR induced UC enhancement in this work, we carry out a comparative study of UC emission measurements in the case of $NaYF_4$ NPs (6 nm) deposited on different substrates as shown in Fig. 2F. Note that the average densities of $NaYF_4$ NPs on the different substrates are nearly the same. It is clear that the typical green and red emissions from $NaYF_4$ NPs are observed under 980 nm excitation, and the intensity ratio of green to red emission (I_{green}/I_{red}) is $\approx$5.5, resulting in a weak green color output (see the inset of Fig. 2F(a)). The UC emissions are significantly improved after coupling with plasmonic nanostructures. For the $NaYF_4$ NPs/$W_{18}O_{49}$ NWs, the overall UCL intensity of Er^{3+} increases 134 times, originating from 244 times in $^2H_{11/2}$-$^4I_{15/2}$, 103 times in $^4S_{3/2}$-$^4I_{15/2}$ and 243 times in $^4F_{9/2}$-$^4I_{15/2}$ transitions. For the $NaYF_4$ NPs/Au NRs, the overall UCL intensity increases 232 times, originating from 388 times in $^2H_{11/2}$-$^4I_{15/2}$, 250 times in $^4S_{3/2}$-$^4I_{15/2}$ and 275 times in $^4F_{9/2}$-$^4I_{15/2}$ transitions. No other emission peaks are observed indicating that the plasmonic-coupling has no essential effect on the UC transition process, and the plasmonic nanoparticles have no characteristic emission relative to UCL, as shown in Fig. 2G(b and c). When coupled with Au/$W_{18}O_{49}$ heterostructures, it is exciting to observe that the overall UC emission is enhanced 443 times (967 times in $^2H_{11/2}$-$^4I_{15/2}$, 390 times in $^4S_{3/2}$-$^4I_{15/2}$ and 552 times in $^4F_{9/2}$-$^4I_{15/2}$ transitions) in the 6 nm $NaYF_4$/Au/$W_{18}O_{49}$ composite film, which is superior to using both the single plasmonic layers, and a bright green emission is also spectacular in the micro-area photograph as seen in the inset of Fig. 2F(d). In addition, the overall UC enhancement is not the simple summation of the two single LSPR effect results, which is consistent with the extinction spectrum results. Fig. 2G further depicts the variation of the enhancement factors for the $NaYF_4$ NPs coupled with different plasmonic layers at different emission wavelengths. It is noteworthy that the spectral distribution of Er^{3+} does not change much in the $NaYF_4$/Au film, and the three emissions contribute equally to the overall UC enhancement. In contrast, the spectral distribution varies significantly in the $NaYF_4$/$W_{18}O_{49}$ and $NaYF_4$/Au/$W_{18}O_{49}$ films as shown in Fig. 2F and G. The luminescence intensity ratios of $^2H_{11/2}$-$^4I_{15/2}$ to $^4S_{3/2}$-$^4I_{15/2}$ (R_{HS}) in the $NaYF_4$/$W_{18}O_{49}$ film increase significantly in comparison to those in the $NaYF_4$/Au film, indicating different populating channels of Er^{3+} in the plasmonic Au and $W_{18}O_{49}$-based films; the easier population of $^2H_{11/2}$ occurs in the $NaYF_4$/$W_{18}O_{49}$ plasmonic hybrids.

To deeply comprehend the electric field enhancement by LSPR coupling between Au NRs and $W_{18}O_{49}$ NWs in the heterostructure film, simulations of the electric field distribution surrounding isolated $W_{18}O_{49}$ NWs, a single Au NR, and a Au NR in contact with a $W_{18}O_{49}$ NW under 980 nm excitation *via* the FDTD method are performed as shown in Fig. 3A. The isolated $W_{18}O_{49}$ NWs are simplified as a bundle-like nanostructure consisting of three nanowires, and the maximum localized

Published on 27 January 2020. Downloaded by Changchun Institute of Optics, Fine Mechanics and Physics, CAS on 4/7/2021 8:22:32 AM.

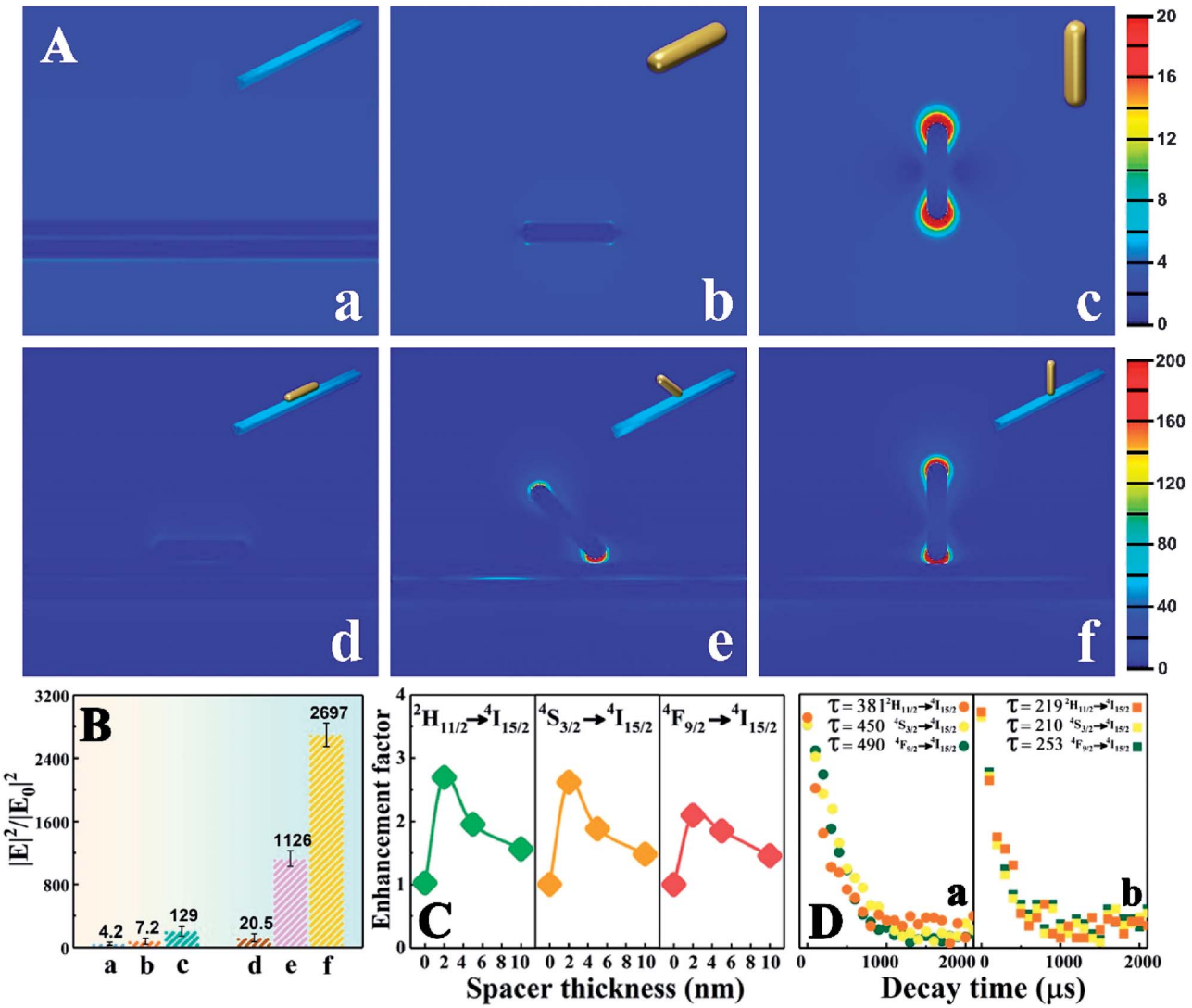

Fig. 3 Electric field distributions of the simulation models of (A) $W_{18}O_{49}$ NWs (a), Au NRs (b and c), and Au NRs/$W_{18}O_{49}$ NWs (d, e and f) under 980 nm excitation. (B) Calculated electromagnetic field strength among $W_{18}O_{49}$ NWs, Au NRs, and Au NRs/$W_{18}O_{49}$ NWs at different contact positions. (C) The enhancement factor of UC luminescence dependent on the thickness of the PVP spacer. (D) Time-resolved decay curves of the (a) $NaYF_4$ NP film and (b) $NaYF_4$ NPs/Au NRs/$W_{18}O_{49}$ NW hybrid film under 980 nm excitation.

electric field enhancement intensity ($|E|^2/|E_0|^2$) of $W_{18}O_{49}$ NWs can reach 4.2 at the plasmonic "hot spots". For the single Au NR, the induced electric field distributions are dependent on the electric field direction. A smooth electric field distribution appears around the Au NR with an $|E|^2/|E_0|^2$ value of about 7.2 for the transverse electric field direction (Fig. 3A(b)). For the longitudinal mode, a dipole-like plasmon resonance as demonstrated by the electric field distribution appears as shown in Fig. 3A(c), and the enhancement factor of $|E|^2/|E_0|^2$ reaches 129. Considering the actual situation in which the Au NRs are deposited randomly on the $W_{18}O_{49}$ NW film, three contact types are selected according to the relative position between Au NRs and the *x*-axis of $W_{18}O_{49}$ NWs, namely parallel, 45° and vertical contact models (Fig. 3A(d–f)). Upon resonance excitation to drive the LSPR coupling of Au/$W_{18}O_{49}$, three of the contact models achieved enhancement of the localized electric fields at the plasmonic "hot spot" regions near the Au/$W_{18}O_{49}$ interface. The distribution of the electric field with a maximum enhancement of 20.5 times at the hot spots is observed when the Au NR is parallel to the *x*-axis of $W_{18}O_{49}$ NWs. Furthermore, when the Au NR touches the *x*-axis of $W_{18}O_{49}$ NWs at an angle of 45°, a 1126 times increase of the electric field intensity is obtained. Finally, the maximum electric field intensity enhancement ($|E|^2/|E_0|^2$) could reach 2697 at the Au/$W_{18}O_{49}$ interface with the vertical contact type. It is confirmed that strong plasmon coupling caused by plasmon hybridization is generated in the Au/$W_{18}O_{49}$ heterostructure under 980 nm excitation, which consequently enhances the extinction performance on the scattering effect of incident light.

The direct contact of plasmonic metal–semiconductor heterostructures with UCNPs results in reverse energy transfer, which is non-radiative energy transfer, thereby quenching the

 This journal is © The Royal Society of Chemistry 2020

Published on 27 January 2020. Downloaded by Changchun Institute of Optics, Fine Mechanics and Physics, CAS on 4/7/2021 8:22:32 AM.

luminescence.[35–38] However, this situation can be ameliorated through employing the polyvinyl pyrrolidone (PVP, K30, M_w = 44 000–54 000) polymer as the intermediate layer to modulate the distance between the plasmonic nanostructure and the UCNPs (Fig. 3C). The optimum thickness of the intermediate layer is 2 nm (see Fig. S5, ESI†), and the enhancement factor begins to attenuate with the increasing thickness due to exceed the acting area of the plasmonic nanostructure to UCNPs. These results indicate that the non-radiative energy transfer process does exist in the 980 nm laser diode excited composite luminescent films, and it is strongly dependent on the distance between luminescent centers and plasmonic nanostructures. When the thickness of the interlayer is appropriate, the UCL of $NaYF_4$ NPs in the composite film could be further enhanced (2.1–2.7 times) due to the suppressed non-radiative energy transfer. Finally, an enhancement up to 1108-fold is achieved for the overall UCL intensity of $NaYF_4$/Au/$W_{18}O_{49}$ compared to that of the pure $NaYF_4$ NPs.

We obtain the UC spectra under excitation with a 980 nm laser with different excitation powers for the transitions of $^2H_{11/2}$, $^4S_{3/2}$, and $^4F_{9/2}$ in various samples (Fig. S6, ESI†). For any multi-photon process, the slope n is approximately equal to the photon number in general. Nevertheless, the slope n deviates from the theoretical photon number, which is attributed to the saturation effect and the local thermal effect.[39–41] It seems that the saturation effect occurs more easily in the hybrid systems (see Fig. S6†), which is attributed to the improved localized excitation electric field due to the modulation of the LSPR effect. The local thermal effect will also influence the slope n. For Er^{3+} ions, the R_{HS} of $^2H_{11/2} \rightarrow {}^4I_{15/2}$ to $^4S_{3/2} \rightarrow {}^4I_{15/2}$ is sensitive to temperature, and the R_{HS} is a critical parameter for studying the thermal effect in UCNPs under exposure to a 980 nm diode laser. We calculate the R_{HS} values of $NaYF_4$ NPs with different sizes deposited on different substrates, and four line charts with the same upward trend show that the photothermal effect around the $NaYF_4$ NPs is remarkable after introducing plasmonic nanoparticles (Fig. S7, ESI†).

In addition to the UCL enhancement as confirmed above, which has been widely accepted, is the excitation enhancement caused by the strengthening of the localized electric field.[33] Considering the impact of the overlapping emission wavelength and LSPR band of the Au NRs/$W_{18}O_{49}$ NW hybrid film on UCL, the effect of matching the LSPR range with the emission wavelength of Yb^{3+}-Er^{3+} has also attracted our attention.[42,43] The plasmonic $W_{18}O_{49}$ nanostructure enhances the UCL due to the strong interaction between LSPR and the UC optical field, which is attributed to the broad LSPR band overlapping both the excitation and emission electric fields of the UCNPs.[44,45] This excellent feature of $W_{18}O_{49}$ is still maintained in the Au/$W_{18}O_{49}$ heterostructures, as shown in the extinction spectra in Fig. 1E. The interactions between the LSPR of Au/$W_{18}O_{49}$ heterostructures and the emission electric field of $NaYF_4$ NPs are assessed through simulating the electric field distributions excited by emission wavelengths at 522, 540, and 654 nm, respectively (Fig. S8, ESI†). The FDTD calculations suggest that enhancement in the emission electric field also occurs near the $NaYF_4$ NPs/Au/$W_{18}O_{49}$ interface with the enhancement factors ranging from 5.8 to 65.5 times at different emission wavelengths. Furthermore, the variation in the rate of the radiation transition is a criterion for determining whether the interaction of LSPR with the emission electric field works or not.[35,36] We determined the fluorescence lifetime of $^2H_{11/2} \rightarrow {}^4I_{15/2}$, $^4S_{3/2} \rightarrow {}^4I_{15/2}$ and $^4F_{9/2} \rightarrow {}^4I_{15/2}$ for the pure $NaYF_4$ NP film and $NaYF_4$ NPs/Au NRs/$W_{18}O_{49}$ NW composite luminescent film (Fig. 3D). The decay curves are presented as exponential decay kinetics as follows:

$$\tau_A = \frac{A_1\tau_1^2 + A_2\tau_2^2}{A_1\tau_1 + A_2\tau_2} \quad (1)$$

According to the emission lifetime (τ_1,τ_2) and the corresponding amplitude (A_1,A_2), the radiative composite of free electrons and the non-radiative composite of charge carriers are estimated to calculate the average fluorescence lifetime of the as-synthesized sample. We compute formula (1) to discover that the average fluorescence lifetime decreases significantly from 450 μs to 210 μs after $NaYF_4$ NP coupling with Au NRs/$W_{18}O_{49}$ NW plasmonic nano-heterostructures, from which it can be concluded that the acceleration of the radiative transition rate induced by dual LSPR of Au NRs/$W_{18}O_{49}$ NWs does indeed contribute to the enhancement of UCL.[32] That is to say, the coupling of the emission wavelength of $NaYF_4$ NPs and LSPR band of Au NRs/$W_{18}O_{49}$ NWs contributes to the enhancement of UCL in this system, although the dominant contribution is still the enhancement of the excitation field.

Based on the above considerations, we propose that the mechanism of the UCL enhancement can be attributed to two aspects: (1) the interaction of the LSPR with the excitation electromagnetic field leading to an enhancement of the localized excitation field strength. A broad and robust plasmonic extinction band is obtained by strong plasmonic-coupling of LSPR with the excitation field between Au NRs and $W_{18}O_{49}$ NWs. The luminescent layer fabricated from 6 nm $NaYF_4$ NPs deposited on the Au/$W_{18}O_{49}$ plasmonic composite film and a thin layer of PVP is inserted to control the interaction distance between plasmonic nanostructures and luminescent emitters. The overall UCL intensity of Er^{3+} increases 1108-fold in the multilayer-structured composite film, which is mainly attributed to the improved localized excitation electric field due to the modulation of LSPR. This is also supported by the simulation of the electric field intensity distribution. (2) The interaction of the LSPR with the emission electromagnetic field resulting in the improved radiative transition rate of emitters. This can be deduced by using the FDTD simulation results and the decrease of the decay time after coupling with the plasmonic Au/$W_{18}O_{49}$ composite film.

The unique electromagnetic field improvement and UC multi-emission enhancement caused by excellent synergetic LSPR properties lead to a new application in fluorescent molecule detection. The SEM picture shows that the Au NRs are densely distributed and intercalated into the $W_{18}O_{49}$ NWs forming the plasmon Au/$W_{18}O_{49}$ composite film. When the $NaYF_4$ NPs deposits on the surface of the Au/$W_{18}O_{49}$ film, the laying of inhomogeneity exists which is caused by the great

Published on 27 January 2020. Downloaded by Changchun Institute of Optics, Fine Mechanics and Physics, CAS on 4/7/2021 8:22:32 AM.

difference in scale and appearance characters between the $NaYF_4$ NPs and the Au/$W_{18}O_{49}$ hybrid, as shown in the Fig. 4A. Thus, plasmon-enhanced UC fluorescence is obtained in the $NaYF_4$/Au/$W_{18}O_{49}$ composite film; meanwhile it has no distinct suppression effect on the SERS signal in this particular multi-layer structure. This could be a new detection method based on a dual role of the plasmon composite film, as the substrates for SERS and efficient UC fluorescence sensing. As a proof of concept, we use R6G as a probe molecule and the $NaYF_4$/Au/$W_{18}O_{49}$ composite film as the substrate to detect R6G qualitatively through SERS signal monitoring and quantitatively though UC fluorescence sensing (Fig. 4A). The SERS spectrum of the R6G solution on the surface of the $NaYF_4$/Au/$W_{18}O_{49}$ film exhibits characteristic vibration characteristics, showing the "fingerprint" characteristic of Raman spectra, of which the Raman band intensity at 610 cm^{-1} (vibration with the highest signal sensitivity) is selected for comparison at various concentrations.[46] Fig. 4B depicts the magnified SERS spectra in the 610 cm^{-1} Raman shift window for 10^{-3} to 10^{-11} M R6G concentrations. The detection limit of the SERS substrate is 10^{-11} M for R6G which affirms the high sensitivity detection of highly diluted samples. The quantitative comparison of SERS intensities related to the concentration of R6G indicates a linear SERS response with the R6G concentration ranging from 10^{-11} to 10^{-7} M (shown in Fig. 4C). The SERS response-concentration linear relationship in a narrow concentration window is similar to that in the relevant literature,[9,47] indicating the limitations of quantitative detection using SERS substrates. Thereby, we carry out fluorescence sensing of the R6G solution in order to achieve quantitative detection and analysis in a wide concentration range. Fig. 4D further exhibits a group of overlapping peaks about the excitation spectrum of R6G and the emission

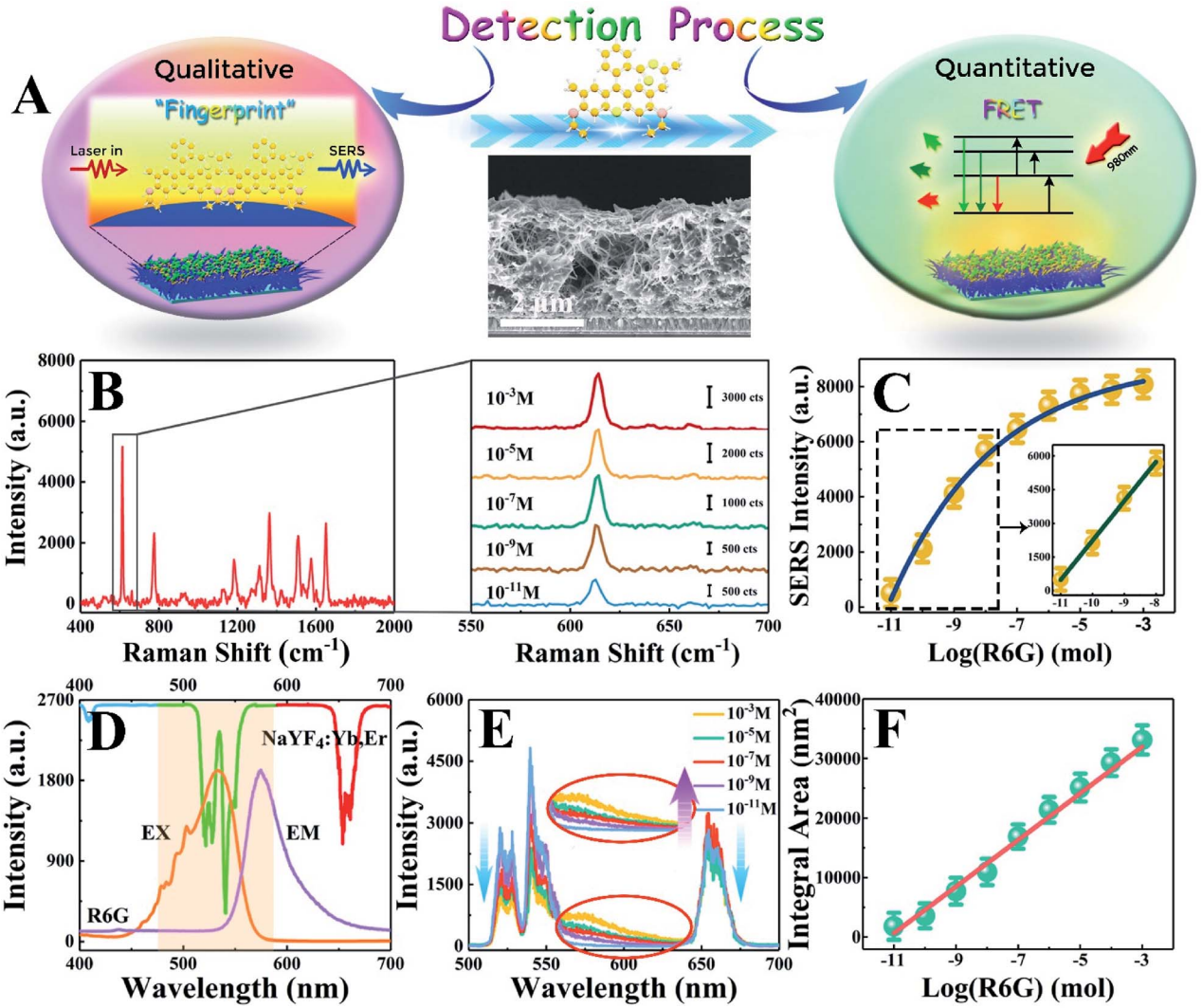

Fig. 4 (A) The diagram of the fluorescent probe molecular detection process. (B) SERS spectra of R6G on the composite Ag NRs/$W_{18}O_{49}$ NW film substrate at concentrations ranging from 10^{-3} to 10^{-11} M at 610 cm^{-1}. (C) The linear relationship of SERS intensity at 610 cm^{-1} with R6G concentration up to 10^{-11} M. (D) The emission spectrum of $NaYF_4$ NPs excited at 980 nm and the absorption and emission spectra of R6G stimulated by 540 nm. (E) Emission spectra of the $NaYF_4$ NPs/Ag NRs/$W_{18}O_{49}$ NW film loaded with a R6G solution. (F) The linear relationship of the emission area ranging from 560 nm to 642 nm with different rhodamine 6G concentrations.

 This journal is © The Royal Society of Chemistry 2020

Published on 27 January 2020. Downloaded by Changchun Institute of Optics, Fine Mechanics and Physics, CAS on 4/7/2021 8:22:32 AM.

spectrum of $NaYF_4$ NPs, which induce fluorescence resonance energy transfer owing to long-distance dipole–dipole interactions for strengthening the emission intensity of fluorescent molecules at low concentrations.[17,18] The characteristic emission peak of the R6G solution shown in Fig. 4D appears in the regular emission spectrum of $NaYF_4$ NPs deposited on the composite film in the excited state when various concentrations of the R6G solution are alternately loaded on the $NaYF_4$/Au/$W_{18}O_{49}$ film (Fig. 4E). With the increase of concentration, the characteristic peak of R6G at 570 nm becomes even more obvious, and the green emission intensity of $NaYF_4$ NPs decreases with a low concentration R6G solution, where the results demonstrate the existence of fluorescence resonance energy transfer. Finally, we confirm that the concentration is linearly related to the integral area of R6G fluorescence emission under the stimulation of ultra-intense emission light ($^2H_{11/2}$-$^4I_{15/2}$, $^4S_{3/2}$-$^4I_{15/2}$) and the linearly correlated concentration extends to 10^{-3} M (Fig. 4F). This dual detection method can offer two functionalities for R6G molecule detection, namely, qualitative detection by SERS and quantitative detection by fluorescence sensing. This detection system has a high sensitivity of 10^{-11} M, a good linear relationship and a wide detection range of 10^{-11} to 10^{-3} M, and thus may have great potential for accurate molecular detection.

Conclusions

In summary, strong plasmonic coupling has been demonstrated in the Au/$W_{18}O_{49}$ heterostructure, in which the localized electric field is dramatically amplified. UC fluorescence of $NaYF_4$:Yb^{3+},Er^{3+} UCNPs is investigated and optimized in the vicinity of the composite plasmonic Au/$W_{18}O_{49}$ nanostructure. Based on the fact that LSPR of the Au/$W_{18}O_{49}$ hybrid matches both the absorption and emission wavelengths of the UCNPs, our work evaluates the influence of the two factors, the excitation and emission electric field effects, in the $NaYF_4$/Au/$W_{18}O_{49}$ hybrid. The results demonstrate that a significant enhancement of UCL is observed by precisely tuning the L-LSPR wavelength of the Au NRs at 980 nm; meanwhile, the interaction distance between the plasmonic nanostructure and the UCNPs emitters is optimized by tuning the emitter particle size from 6 to 50 nm and the separation distance in the range from 2 to 10 nm in order to overcome fluorescence quenching. A remarkable enhancement up to 1108 fold is achieved for the overall UCL intensity of Er^{3+} in the dual LSPR coupling mode of the Au NRs/$W_{18}O_{49}$ NW heterostructure. Finally, the $NaYF_4$/Au/$W_{18}O_{49}$ composite luminescent film is used in the qualitative detection of fluorescent molecules, and then the fluorescent molecules are quantitatively measured based on induced ultra-strong emission, which widens the scope for solving the problem of fluorescent molecule detection.

Conflicts of interest

There are no conflicts to declare.

Acknowledgements

This work was supported by the National Natural Science Foundation of China (Grant no. 11974069, 11904046, 11874101, 61805033 and 11874055), National Special Support Program for High-level Personnel Recruitment, Xingliao Talents Program of Liaoning Province (XLYC1902113), Program for Liaoning Innovation Team in University (LT2016011), Natural Science Foundation of Liaoning Province (Grant nos. 20170540200 and 20180550100), Science and Technique Foundation of Dalian (Grant no. 2017RD12), Open Fund of the State Key Laboratory on Integrated Optoelectronics (Grant no. IOSKL2019KF10), and Fundamental Research Funds for the Central Universities (Grant no. 0220-110010).

Notes and references

1 F. Pincella, K. Isozaki and K. Miki, *Light: Sci. Appl.*, 2014, **3**, e133.
2 J. Zhang, Z. Hao, J. Li, X. Zhang, Y. Luo and G. Pan, *Light: Sci. Appl.*, 2015, **4**, e239.
3 D. Zhou, D. Liu, J. Jin, X. Chen, W. Xu, Z. Yin, G. Pan, D. Li and H. Song, *J. Mater. Chem. A*, 2017, **5**, 16559–16567.
4 S. Lee, J. Jo, J. Park, S. Lee and J. Jiang, *J. Mater. Chem. A*, 2018, **6**, 20939–20946.
5 S. Zhao, D. Xia, R. Zhao, H. Zhu, Y. Zhu, Y. Xiong and Y. Wang, *Nanotechnology*, 2017, **28**, 015601.
6 S. Jayabal, R. Sathiyamurthi and R. Ramaraj, *J. Mater. Chem. A*, 2014, **2**, 8918–8925.
7 H. Wang, X. Han, X. Ou, C. S. Lee, X. Zhang and S. T. Lee, *Nanoscale*, 2013, **5**, 8172–8176.
8 X. He, H. Wang, Z. Li, D. Chen, J. Liu and Q. Zhang, *Nanoscale*, 2015, **7**, 8619–8626.
9 H. K. Lee, Y. H. Lee, Q. Zhang, I. Y. Phang, J. M. Tan, Y. Cui and X. Y. Ling, *ACS Appl. Mater. Interfaces*, 2013, **5**, 11409–11418.
10 R. Pan, Y. Yang, Y. Wang, S. Li, Z. Liu, Y. Su, B. Quan, Y. Li, C. Gu and J. Li, *Nanoscale*, 2018, **10**, 3171–3180.
11 W. H. Hsiao, H. Y. Chen, Y. C. Yang, Y. L. Chen, C. Y. Lee and H. T. Chiu, *ACS Appl. Mater. Interfaces*, 2011, **3**, 3280–3284.
12 M. Mulvihill, A. Tao, K. Benjauthrit, J. Arnold and P. Yang, *Angew. Chem., Int. Ed.*, 2008, **47**, 6456–6460.
13 Q. Chen, X. Xie, B. Huang, L. Liang, S. Han, Z. Yi, Y. Wang, Y. Li, D. Fan, L. Huang and X. Liu, *Angew. Chem., Int. Ed.*, 2017, **56**, 7605–7609.
14 B. Tandon, A. Agrawal, S. Heo and D. J. Milliron, *Nano Lett.*, 2019, **19**, 2012–2019.
15 J. S. DuChene, B. C. Sweeny, A. C. Johnston-Peck, D. Su, E. A. Stach and W. D. Wei, *Angew. Chem., Int. Ed.*, 2014, **53**, 7887–7891.
16 S. K. Cushing, J. Li, F. Meng, T. R. Senty, S. Suri, M. Zhi, M. Li, A. D. Bristow and N. Wu, *J. Am. Chem. Soc.*, 2012, **134**, 15033–15041.
17 S. Xu, W. Xu, Y. Wang, S. Zhang, Y. Zhu, L. Tao, L. Xia, P. Zhou and H. Song, *Nanoscale*, 2014, **6**, 5859–5870.
18 R. Chen, V. D. Ta, F. Xiao, Q. Zhang and H. Sun, *Small*, 2013, **9**, 1052–1057.

Published on 27 January 2020. Downloaded by Changchun Institute of Optics, Fine Mechanics and Physics, CAS on 4/7/2021 8:22:32 AM.

19 J. Liu, Y. Liu, Q. Liu, C. Li, L. Sun and F. Li, *J. Am. Chem. Soc.*, 2011, **133**, 15276–15279.
20 M. Pelton, *Nat. Photonics*, 2015, **9**, 427–435.
21 H. Dong, S. R. Du, X. Y. Zheng, G. M. Lyu, L. D. Sun, L. D. Li, P. Z. Zhang, C. Zhang and C. H. Yan, *Chem. Rev.*, 2015, **115**, 10725–10815.
22 H. Cheng, T. Kamegawa, K. Mori and H. Yamashita, *Angew. Chem., Int. Ed.*, 2014, **53**, 2910–2914.
23 B. M. van der Ende, L. Aarts and A. Meijerink, *Phys. Chem. Chem. Phys.*, 2009, **11**, 11081–11095.
24 Y. Tang, H. Liu, J. Gao, X. Liu, X. Gao, X. Lu, G. Fang, J. Wang and J. Li, *Talanta*, 2018, **181**, 95–103.
25 X. Fang, H. Song, L. Xie, Q. Liu, H. Zhang, X. Bai, B. Dong, Y. Wang and W. Han, *J. Chem. Phys.*, 2009, **131**, 054506.
26 F. Kang, J. He, T. Sun, Z. Y. Bao, F. Wang and D. Y. Lei, *Adv. Funct. Mater.*, 2017, **27**, 1701842.
27 C. Ng, L. W. Yap, A. Roberts, W. Cheng and D. E. Gómez, *Adv. Funct. Mater.*, 2017, **27**, 1604080.
28 W. R. Erwin, H. F. Zarick, E. M. Talbert and R. Bardhan, *Energy Environ. Sci.*, 2016, **9**, 1577–1601.
29 H. F. Zarick, W. R. Erwin, A. Boulesbaa, O. K. Hurd, J. A. Webb, A. A. Puretzky, D. B. Geohegan and R. Bardhan, *ACS Photonics*, 2016, **3**, 385–394.
30 J. DuChene, B. Sweeny, A. Johnston-Peck, D. Su, E. Stach and W. Wei, *Angew. Chem., Int. Ed.*, 2014, **53**, 7887–7891.
31 P. Zilio, M. Dipalo, F. Tantussi, G. Messina and F. Angelis, *Light: Sci. Appl.*, 2017, **6**, e17002.
32 E. Yablonovitch, *Phys. Rev. Lett.*, 1987, **58**, 2059–2062.
33 X. Liu and D. Yuan Lei, *Sci. Rep.*, 2015, **5**, 15235.
34 X. Chen, W. Xu, L. Zhang, X. Bai, S. Cui, D. Zhou, Z. Yin, H. Song and D.-H. Kim, *Adv. Funct. Mater.*, 2015, **25**, 5462–5471.
35 Q.-C. Sun, H. Mundoor, J. C. Ribot, V. Singh, I. I. Smalyukh and P. Nagpal, *Nano Lett.*, 2013, **14**, 101–106.
36 J. Shang, X. Xu, K. Liu, Y. Bao and B. Dong, *J. Alloys Compd.*, 2019, **785**, 610–615.
37 D. Zhou, D. Liu, W. Xu, Z. Yin, X. Chen, P. Zhou, S. Cui, Z. Chen and H. Song, *ACS Nano*, 2016, **10**, 5169–5179.
38 Y. Xie, L. Carbone, C. Nobile, V. Grillo, S. D'Agostino, F. Sala, C. Giannini, D. Altamura, C. Oelsner, C. Kryschi and P. Cozzoli, *ACS Nano*, 2013, **7**, 7352–7369.
39 W. Xu, T. K. Lee, B.-S. Moon, H. Song, X. Chen, B. Chun, Y.-J. Kim, S. K. Kwak, P. Chen and D.-H. Kim, *Adv. Opt. Mater.*, 2018, **6**, 1701119.
40 Z. Yin, H. Li, W. Xu, S. Cui, D. Zhou, X. Chen, Y. Zhu, G. Qin and H. Song, *Adv. Mater.*, 2016, **28**, 2518–2525.
41 X. Ma, Y. Dai, L. Yu and B. Huang, *Light: Sci. Appl.*, 2016, **5**, e16017.
42 L. Brus, *Acc. Chem. Res.*, 2008, **41**, 1742–1749.
43 A. Suarez-Garcia, R. Serna, M. Jiménez, C. Afonso and I. Vickridge, *Appl. Phys. Lett.*, 2004, **84**, 2151–2153.
44 Y. Ji, W. Xu, D. Li, D. Zhou, X. Chen, N. Ding, J. Li, N. Wang, X. Bai and H. Song, *Nano Energy*, 2019, **61**, 211–220.
45 D. Zhou, D. Li, X. Zhou, W. Xu, X. Chen, D. Liu, Y. Zhu and H. Song, *ACS Appl. Mater. Interfaces*, 2017, **9**, 35226–35233.
46 Z. Huang, G. Meng, Q. Huang, Y. Yang, C. Zhu and C. Tang, *Adv. Mater.*, 2010, **22**, 4136–4139.
47 X. Li, H. K. Lee, I. Y. Phang, C. K. Lee and X. Y. Ling, *Anal. Chem.*, 2014, **86**, 10437–10444.

This journal is © The Royal Society of Chemistry 2020